A98-31496 ICAS-98-2,2,3

ADAPTIVE MESH REFINEMENT ON THE SOLUTION OF TWO-DIMENSIONAL VISCOUS AEROSPACE PROBLEMS

Heidi Korzenowski*, Edisson S.G. Maciel*
Instituto Tecnológico de Aeronáutica
CTA/ITA/IEAA
12228-900 – São José dos Campos – SP – BRAZIL

João Luiz F. Azevedo†
Instituto de Aeronáutica e Espaço
CTA/IAE/ASE-N
12228-904 – São José dos Campos – SP – BRAZIL

Abstract

A study of adaptive mesh refinement and of high resolution flux-vector splitting schemes on the solution of 2-D aerospace problems is described. The emphasis of the work is in developing the capability of accurately simulating realistic viscous flows of aerospace interest. The governing equations are discretized in a cell centered, finite volume procedure for unstructured triangular grids. Spatial discretization considers three different schemes, including a centered and two upwind schemes. Time march uses an explicit, 2nd-order accurate, 5-stage Runge-Kutta time stepping scheme. Results are presented for adaptive inviscid simulations of the flow in a hypersonic inlet configuration. Viscous simulations have considered airfoil flows, transonic convergent-divergent nozzle cases and the hypersonic inlet configuration. For all cases considered, the results have shown good qualitative agreement with the expected flow features.

Introduction

The recent progress in Computational Fluid Dynamics (CFD) has made these techniques attractive tools for real life problems in aeronautical and aerospace applications. However, several of these applications require the use of efficient and robust algorithms as well as efficient procedures to obtain adequate meshes. On the other hand, these accurate solutions usually involve sufficiently refined meshes and, despite the mesh refinement, the computational cost must be maintained within acceptable levels. The use of unstructured mesh techniques try to accomplish this goal by providing an environment suitable for automatic grid refinement procedures. Adaptive refinement adds computational points only where they are necessary and, therefore, obtain the lowest cost solution for a given required accuracy level.

The present work is concerned with the implementation and validation of unstructured grid, mesh refinement techniques for two-dimensional inviscid and viscous flow problems of aerospace interest. The present development should be seen as an evolutionary step towards the desired three-dimensional capability. The goal was to develop all the criteria necessary to construct adaptive meshes suitable to the desired applications in the 2-D case, for computational cost reasons. Moreover, there was also interest in obtaining spatial discretization schemes which were sufficiently robust in order to treat flows from the transonic regime up to hypersonic speeds. In this context, the capability here implemented was tested on standard two-dimensional cases of interest, including transonic nozzles, airfoils and a hypersonic inlet configuration.

The present approach discretized the Navier-Stokes equations in conservative form in a cell centered, finite volume context considering an unstructured grid made up of triangles. The spatial discretization of the inviscid terms was implemented using both a centered scheme[1, 2] and, also, a few upwind schemes based on the flux-vector splitting concept. For the flux-vector splitting cases, both a van Leer[3, 4] and a Liou[5, 6] formulation have been tested. Results with the first-order and the second-order implementations have been obtained. The second-order flux-vector splitting schemes have used a MUSCL-type extrapolation[7, 8] in order to determine left and right states at the interfaces. Several limiters have also been tested in connection with the second-order upwind schemes, including the minmod, superbee, van Leer and van Albada limiters[8]. The discretization of the viscous terms was always equivalent to a central difference scheme. Time integration used an explicit, second-order accurate, hybrid method which evolved from the consideration of Runge-Kutta time stepping schemes[9]. Spatially variable time stepping and implicit residual smoothing procedures[9] were implemented to accelerate convergence

*Graduate Student.

†Head, Aeroelasticity & CFD Sections, Space Systems Division.

21st ICAS Congress
13-18 September 1998
Melbourne, Australia

to steady state solutions.

Adaptive mesh refinement, based on a sensor of flow property gradients, was performed to obtain a better resolution of strong discontinuities. The automated adaptive environment consisted of a mesh enrichment procedure that divides each identified triangle which needs refinement into four new triangles by adding a new point on each face. In order to avoid hanging nodes, the triangles that had only one face marked should be divided by halving. The properties of each new triangle were set equal to those of the original one in order to restart the time iteration process. A density gradient-based sensor has been used in this work. The forthcoming sections will briefly describe the theoretical formulation and numerical implementation details. Several case studies are discussed in an attempt to illustrate the capability implemented. Finally, a critical discussion of the present status of the work is presented together with a perspective for future developments.

Theoretical Formulation

The 2-D time-dependent, compressible Navier-Stokes equations can be written in conservation-law form as

$$\frac{\partial Q}{\partial t} + \frac{\partial (E_e - E_v)}{\partial x} + \frac{\partial (F_e - F_v)}{\partial y} = 0 \,. \qquad (1)$$

Here, Q is the vector of conserved variables, defined as

$$Q = \left[\begin{array}{cccc} \rho & \rho u & \rho v & e \end{array} \right]^T \,, \qquad (2)$$

where ρ is the fluid density, u and v are the Cartesian velocity components, and e is the total energy per unit of volume. The flux vectors, E_e, E_v, F_e and F_v, can be defined as

$$E_e = \left\{ \begin{array}{c} \rho u \\ \rho u^2 + p \\ \rho u v \\ (e+p)u \end{array} \right\} \,, \quad F_e = \left\{ \begin{array}{c} \rho v \\ \rho u v \\ \rho v^2 + p \\ (e+p)v \end{array} \right\} \,,$$

$$E_v = \frac{1}{Re} \left\{ \begin{array}{c} 0 \\ \tau_{xx} \\ \tau_{xy} \\ \tau_{xx} u + \tau_{xy} v - q_x \end{array} \right\} \,, \qquad (3)$$

$$F_v = \frac{1}{Re} \left\{ \begin{array}{c} 0 \\ \tau_{xy} \\ \tau_{yy} \\ \tau_{xy} u + \tau_{yy} v - q_y \end{array} \right\} \,.$$

In the previous expressions, the components of the viscous stress tensor can be written as

$$\begin{aligned} \tau_{xx} &= 2\mu \frac{\partial u}{\partial x} - \frac{2}{3}\mu \left(\frac{\partial u}{\partial x} + \frac{\partial v}{\partial y} \right) \,, \\ \tau_{xy} &= \mu \left(\frac{\partial u}{\partial y} + \frac{\partial v}{\partial x} \right) \,, \qquad (4) \\ \tau_{yy} &= 2\mu \frac{\partial v}{\partial y} - \frac{2}{3}\mu \left(\frac{\partial u}{\partial x} + \frac{\partial v}{\partial y} \right) \,. \end{aligned}$$

The components of the heat flux vector can be obtained by the Fourier law of heat conduction, and they can be written in the present context as

$$q_x = \frac{\gamma \mu}{Pr} \frac{\partial e_i}{\partial x} \,, \quad q_y = \frac{\gamma \mu}{Pr} \frac{\partial e_i}{\partial y} \,. \qquad (5)$$

The specific internal energy, e_i, can be related to the total energy per unit of volume, e, as

$$e_i = \frac{e}{\rho} - \frac{1}{2}\left(u^2 + v^2\right) \,. \qquad (6)$$

Moreover, the present work assumed that the ideal equation of state could be used and, hence, the pressure, p, can be written as

$$p = (\gamma - 1)\, \rho e_i \,, \qquad (7)$$

where γ is the ratio of specific heats. The Reynolds number was defined in the present context as

$$Re = \frac{\rho a \ell}{\mu} \,, \qquad (8)$$

where a is the speed of sound, ℓ is a characteristic length of the geometry under study, and μ is the fluid dynamic viscosity coefficient. Finally, Pr is the Prandtl number.

The Euler equations can be simply obtained by neglecting the viscous terms in Eq. (1), i.e., by neglecting the E_v and F_v flux vectors. Hence, the following theory will be presented for the general case of the Navier-Stokes equations. Moreover, the discussion of the spatial discretization of these equations will be conducted considering separately viscous and inviscid terms.

If the equations are discretized using a cell centered based finite volume procedure, the discrete vector of conserved variables, Q_i, is defined as an average over the i-th control volume as

$$Q_i = \frac{1}{V_i} \int_{V_i} Q \, dV \,. \qquad (9)$$

In this context, the discrete flow variables can be assumed as attributed to the centroid of each cell if necessary. With the previous definition of Q_i, Eq. (1) can be integrated over the i-th control volume and, after the use of the divergence theorem, it can be rewritten as

$$\begin{aligned} \frac{\partial}{\partial t}\left(V_i Q_i\right) &+ \int_{S_i} \left(E_e \, dy - F_e \, dx\right) \\ &- \int_{S_i} \left(E_v \, dy - F_v \, dx\right) = 0 \,. \qquad (10) \end{aligned}$$

Numerical Implementation

This section describes the most relevant aspects associated with the discretization of the Euler or the Navier-Stokes equations in the present context. Both spatial and temporal discretizations are discussed, as well as aspects related to the grid adaptation procedure here adopted.

Spatial Discretization of Inviscid Terms

The convective operator, $C_{conv}(Q_i)$, corresponds to the spatial discretization of the inviscid terms in the Navier-Stokes equations, i.e.,

$$C_{conv}(Q_i) \cong \int_{S_i} (E_e\, dy - F_e\, dx) \ . \qquad (11)$$

Since the present work used a cell centered approach, the control volume used for the integration of the governing equations is composed of the triangular cells themselves, regardless of the type of spatial discretization algorithm used for the inviscid terms. In the present case, both centered and upwind schemes have been implemented, in an attempt to compare their relative advantages.

In the centered scheme case, the convective operator is defined as[1, 2]

$$C_{conv}(Q_i) = \sum_{k=1}^{3} [E_e(Q_{ik})\, \Delta y_{ik} - F_e(Q_{ik})\, \Delta x_{ik}] \ . \qquad (12)$$

In this expression, Q_{ik} is the arithmetic average of the conserved properties in the cells which share the ik interface, where i is the i-th control volume and k is its neighbor. Moreover, the k summation is performed over the three neighbors of the i-th triangle. The terms Δx_{ik} and Δy_{ik} are calculated as

$$\Delta x_{ik} = (y_{k2} - y_{k1}), \qquad \Delta y_{ik} = (x_{k2} - x_{k1}) \ , \qquad (13)$$

where the points (x_{k1}, y_{k1}) and (x_{k2}, y_{k2}) are the vertices which define the interface between cells i and k.[10]

For the case of the upwind schemes, the convective operator can be written as

$$C_{conv}(Q_i) = \sum_{k=1}^{3} [E_{ik}\, \Delta y_{ik} - F_{ik}\, \Delta x_{ik}] \ . \qquad (14)$$

The various terms have the same meaning as before, except that, in the present context, the inviscid interface fluxes E_{ik} and F_{ik} can be written, in the general case, as

$$\begin{aligned} E_{ik} &= E_e^+(Q_L) + E_e^-(Q_R) \ , \\ F_{ik} &= F_e^+(Q_L) + F_e^-(Q_R) \ . \end{aligned} \qquad (15)$$

Here, Q_L and Q_R are the left and right states at the ik interface, and $E_e^{\pm}$ and $F_e^{\pm}$ are split fluxes computed according to the particular scheme chosen. Two different upwind schemes have been implemented in the present work, namely the van Leer flux-vector splitting scheme[3, 4] and the AUSM$^+$ scheme presented by Liou[5, 6]. Moreover, the upwind schemes were implemented both in their 1st- and 2nd-order versions, which essentially amounts to assume piecewise constant or piecewise linear variation of flow properties within each cell, respectively. A detailed discussion of the form in which these schemes were implemented in the current unstructured context is presented in Ref. [11], and it will not be repeated here. The interested reader is referred to the cited reference for all the specific implementation details.

It is worth emphasizing, however, that the Q_L and Q_R properties are simply taken as the conserved properties for the two triangles which share the particular interface, for the 1st-order upwind implementation. For the 2nd-order schemes, these left and right interface properties are obtained from a MUSCL-type reconstruction[4, 7] of primitive variables on either side of the interface. The linearly reconstructed states must be limited[8] in order to avoid the creation of new local extrema. Several limiters have been implemented in the code developed, including the minmod, superbee, van Leer and van Albada limiters[8]. However, all 2nd-order upwind results here reported have used the minmod limiter. Previous experience[12] has indicated that the other limiters may not converge to machine zero for the cases of interest in the present work.

Artificial Dissipation

The upwind schemes automatically provide the artificial dissipation terms necessary to maintain nonlinear stability. However, the centered scheme does requires the explicit addition of an artificial dissipation operator in order to guarantee numerical stability during the convergence process. The artificial dissipation terms implemented in the present work used undivided Laplacian and biharmonic operators in order to provide stability for the scheme in the presence of flow discontinuities and to avoid odd-even uncoupling of the solutions, respectively. The particular implementation of the artificial dissipation operator, $D(Q_i)$, adopted here is based on the work of Mavriplis[13]. In this case, the artificial dissipation terms are weighted by an average of the spectral radii of the inviscid flux Jacobian matrices computed in the direction normal to the corresponding control volume face.

Hence, the artificial dissipation operator, $D(Q_i)$, can be written as

$$D(Q_i) = d^{(2)}(Q_i) - d^{(4)}(Q_i) \ , \qquad (16)$$

where $d^{(2)}(Q_i)$ represents the undivided Laplacian operator and $d^{(4)}(Q_i)$ is the biharmonic operator. The undivided Laplacian operator is responsible for providing stability in regions of discontinuities, and this operator can be written as

$$d^{(2)}(Q_i) = \sum_{k=1}^{3} \frac{\epsilon_{ik}^{(2)}}{2} (A_i + A_k)(Q_k - Q_i) \ . \qquad (17)$$

The biharmonic operator is responsible for providing background dissipation and for avoiding odd-even decoupling of the solutions. This operator was implemented as

$$d^{(4)}(Q_i) = \sum_{k=1}^{3} \frac{\epsilon_{ik}^{(4)}}{2} (A_i + A_k)(\nabla^2 Q_k - \nabla^2 Q_i) \ , \qquad (18)$$

where

$$\nabla^2 Q_i = \sum_{k=1}^{3} (Q_k - Q_i) \ . \qquad (19)$$

In the construction of the biharmonic operator, the contribution of the k-th cell is neglected whenever k represents a "ghost" control volume.

The $\epsilon_{ik}^{(2)}$ and $\epsilon_{ik}^{(4)}$ terms are defined as

$$\begin{aligned} \epsilon_{ik}^{(2)} &= K^{(2)} \max(\nu_i \ , \ \nu_k) \ , \\ \epsilon_{ik}^{(4)} &= \max\left[0 \ , \ \left(K^{(4)} - \epsilon_{ik}^{(2)}\right)\right] \ . \end{aligned} \tag{20}$$

The pressure gradient sensor is written as

$$\nu_i = \frac{\sum_{k=1}^{3} |p_k - p_i|}{\sum_{k=1}^{3} (p_k + p_i)} \ , \tag{21}$$

and this term is constructed such as to identify regions of high gradients (e.g., shock waves). The $K^{(2)}$ and $K^{(4)}$ constants have assumed the typical values of 1/4 and 3/256, respectively, usually suggested in the literature[2]. The scaling terms, A_i, are constructed proportional to the maximum eigenvalue of the Euler equations in the direction normal to the particular edge. The contributions of each edge are added up for all sides of the control volume. Hence, these terms can be written as

$$A_i = \sum_{k=1}^{3} \left[|u_{ik} \, \Delta y_{ik} - v_{ik} \, \Delta x_{ik}| + a_{ik} \sqrt{\Delta x_{ik}^2 + \Delta y_{ik}^2} \right] , \tag{22}$$

where u_{ik}, v_{ik} and a_{ik} are calculated as the arithmetic average of the values of these properties in the i-th volume and its k-th neighboring volume.

Spatial Discretization of Viscous Terms

The viscous operator, $C_{visc}(Q_i)$, corresponds to the spatial discretization of the viscous terms in the Navier-Stokes equations. Therefore, according to Eq. (10), one could write

$$C_{visc}(Q_i) \cong \int_{S_i} (E_v \, dy - F_v \, dx) \ . \tag{23}$$

In the present work, the viscous terms are discretized in the usual way by the equivalent of a central difference-type scheme. Hence, the viscous operator can be written as

$$C_{visc}(Q_i) = \sum_{k=1}^{3} [E_v(Q_{ik}) \, \Delta y_{ik} - F_v(Q_{ik}) \Delta x_{ik}] \ . \tag{24}$$

As before, Q_{ik} is the arithmetic average of the conserved properties in the cells which share the ik interface.

The evaluation of the viscous flux vectors involves derivatives of the flow variables. The procedure adopted in the present work consisted in evaluating these derivatives, for each control volume, by the application of Green's theorem[14]. In this context, the derivative calculation is actually replaced by a line integral evaluation, in the 2-D case, around an appropriate control volume. The triangular control volumes themselves were selected for this integration in the present work. The discrete values of the derivatives are, therefore, assumed constant within each control volume, similarly to the approach adopted for the conserved variables. The interface values of the derivatives are also taken as the arithmetic average of the corresponding derivative values in the two control volumes which share the interface under consideration.

Temporal Discretization

After the complete spatial discretization process, the governing equations indicated in Eq. (10) can be rewritten as

$$\frac{d(V_i Q_i)}{dt} + C_{conv}(Q_i) - C_{visc}(Q_i) - D(Q_i) = 0 \ . \tag{25}$$

Clearly, if only the Euler equations are being considered, the $C_{visc}(Q_i)$ operator is neglected. Similarly, if the discretization of the inviscid terms uses an upwind scheme, the artificial dissipation operator, $D(Q_i)$, is set identically equal to zero.

Time integration of these equations is performed through a 2nd-order, 5-stage, explicit Runge-Kutta time-stepping scheme[2, 13]. The time integration method can be written as

$$\begin{aligned} Q_i^{(0)} &= Q_i^n \ , \\ Q_i^{(1)} &= Q_i^{(0)} - \alpha_1 \frac{\Delta t_i}{V_i} \left[C\left(Q_i^{(0)}\right) - D\left(Q_i^{(0)}\right) \right] , \\ Q_i^{(2)} &= Q_i^{(0)} - \alpha_2 \frac{\Delta t_i}{V_i} \left[C\left(Q_i^{(1)}\right) - D\left(Q_i^{(0)}\right) \right] , \\ Q_i^{(3)} &= Q_i^{(0)} - \alpha_3 \frac{\Delta t_i}{V_i} \left[C\left(Q_i^{(2)}\right) - D\left(Q_i^{(2)}\right) \right] , \\ Q_i^{(4)} &= Q_i^{(0)} - \alpha_4 \frac{\Delta t_i}{V_i} \left[C\left(Q_i^{(3)}\right) - D\left(Q_i^{(2)}\right) \right] , \\ Q_i^{(5)} &= Q_i^{(0)} - \alpha_5 \frac{\Delta t_i}{V_i} \left[C\left(Q_i^{(4)}\right) - D\left(Q_i^{(4)}\right) \right] , \\ Q_i^{n+1} &= Q_i^{(5)} \ . \end{aligned} \tag{26}$$

Here, for easiness of writing, $C(Q_i) = C_{conv}(Q_i) - C_{visc}(Q_i)$. Moreover, the α coefficients were taken as

$$\alpha_1 = \frac{1}{4} \ , \ \alpha_2 = \frac{1}{6} \ , \ \alpha_3 = \frac{3}{8} \ , \ \alpha_4 = \frac{1}{2} \ , \ \alpha_5 = 1 \ , \tag{27}$$

as suggested in the literature[1, 2]. According to Swanson and Radespiel[14], for the Navier-Stokes equations, the artificial dissipation terms should be evaluated only at odd stages of the time-stepping process. This has the objective of obtaining CPU time economy and better stability conditions based on the hyperbolic/parabolic features of the Navier-Stokes equations. In the Euler cases, the artificial dissipation operator is only evaluated in the first and second stages of the time-stepping method, as suggested in Ref. [9]. With regard to artificial dissipation evaluation, the previous equations indicated the procedure adopted for the viscous flow simulation cases.

Since all applications considered in the present work dealt with steady state calculations, there was interest in implementing convergence acceleration techniques.

Hence, a spatially variable time step, for each computational mesh cell, was used. The basic idea with this procedure is to maintain a constant CFL number in the complete calculation domain, allowing the use of adequate time steps for each specific mesh region during the convergence process. In this way, and according to the CFL definition, it is possible to write

$$\Delta t_{\text{cell}} = \frac{\text{CFL}\ \Delta s_{\text{cell}}}{c_{\text{cell}}} \ . \qquad (28)$$

Here, CFL is the Courant number, Δs_{cell} is a characteristic length of the mesh, and c_{cell} is a characteristic speed of information transport in the flow. In the present finite volume formulation, Δs_{cell} was chosen as the smallest between the smallest cell centroid-neighboring centroid distance and the smallest cell side length. Moreover, the characteristic speed was taken as $c_{\text{cell}} = (\sqrt{u^2+v^2}+a)_{\text{cell}}$. One should observe that this is the maximum possible characteristic speed for the Euler terms in the governing equations.

Grid Refinement Strategy

The grid adaptation procedure implemented in the present work uses a sensor based on flow property gradients. The general definition of the sensor adopted in the present case could be expressed as

$$(\text{sensor})_i = \left\{ \max_n \left[\frac{|\nabla \phi_n|}{|\phi_{n_{\max}} - \phi_{n_{\min}}|} \right] \right\}_i , \qquad (29)$$

$$\text{where} \quad \phi_n = (\rho, p, u, v, T) \ ,$$

and $\phi_{n_{\max}}$ and $\phi_{n_{\min}}$ are the maximum and the minimum values of the ϕ_n property in the flowfield. Despite this general definition, and despite having implemented the complete sensor calculation as indicated in the above equation, all results presented in this work have used a sensor based on density gradients, i.e., $\phi_n = \rho$.

The first step of the adaptive procedure is to compute the flow on an existing coarse mesh. With this preliminary solution, one can calculate the sensor as previously described. The code marks all triangles in which the sensor exceeds some specified threshold value (the threshold value will be denoted Γ in the present paper), and the marked triangles are refined. A new finer mesh is then constructed by enrichment of the original coarse grid.

The mesh enrichment procedure consists of introducing an additional node for each side of a triangle marked for refinement. For interior sides, this additional node is placed at the mid-point of the side whereas, for boundary sides, it is necessary to refer to the boundary definition to ensure that the new node is placed on the true boundary. After this initial pass, the code has to search all triangles to identify cells that have two or three divided sides. Each of these cells is subdivided into four new triangles. This subdivision may eventually mark new faces. Therefore, this process has to be performed until there are no triangles with more than one marked face. In order to avoid hanging nodes, the triangles that have one marked face should be divided by halving. Figure 1 illustrates the three possible ways of triangle subdivision.

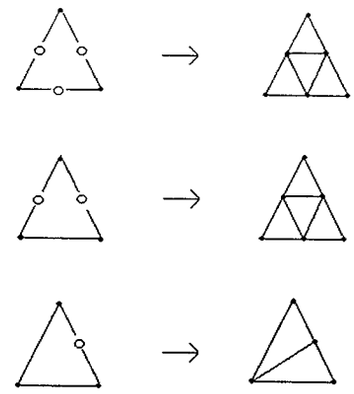

Figure 1: Schematic representation of the three possible triangle subdivision processes.

The second part of the refinement process consists of identifying all triangles which were refined by halving. This information is stored for the next refinement step because, if there is again an attempt to subdivide these triangles by halving, this is not allowed. The experience has shown that repeated triangle division by halving has a strong detrimental effect in mesh quality. Therefore, if the next refinement step tries to divide by halving a triangle which was obtained by a previous division by halving, the logic in the code forces the original triangle to be divided into four new triangles before the refinement procedure is allowed to continue. When the mesh enrichment procedure has been completed, the new control volumes receive the property values of their "father" triangle and the flow solver is re-started.

Results and Discussion

The present work considered the simulation of external flow over an airfoil and internal flows in a convergent-divergent nozzle and in a hypersonic inlet configuration. For the external flow case and for the hypersonic inlet cases, state variables were nondimensionalized with respect to freestream properties. For the transonic convergent-divergent nozzle case, flow variables were made dimensionless with respect to stagnation properties. Moreover, all computational cases considered steady state calculations and the convergence criterion adopted was to require that the maximum residue in the calculation domain was smaller than 10^{-6}.

Inviscid Test Cases

The results obtained for an inviscid flow considered the simulation of the flow in a hypersonic inlet configuration. An entrance Mach number equal to 16 was considered. The fluid was treated as a perfect gas, and no chemistry was taken into account. The purpose of these simulations was to compare the different schemes, previously discussed, applied to high Mach number flows in order

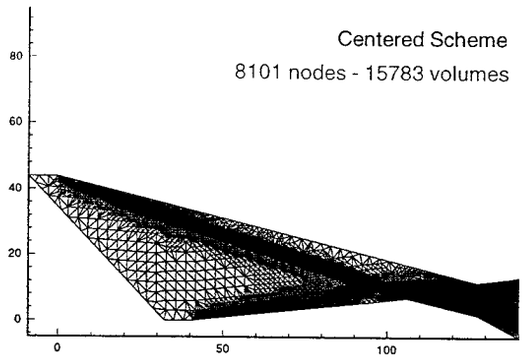

Figure 2: Adaptive mesh obtained using the 1st-order van Leer scheme.

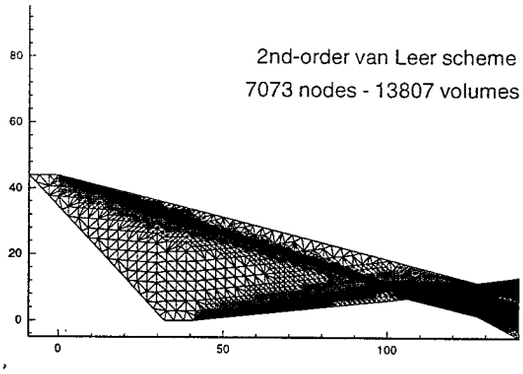

Figure 3: Adaptive mesh obtained using the 2nd-order van Leer scheme.

to verify if they were able to represent the flow features, such as strong shocks, shock reflections and interactions, and expansion regions.

To analyse the different schemes, an adaptive refinement process was used with a sensor based on density gradients. The initial mesh had 399 nodes and 683 volumes. Figures 2, 3, 4 and 5 present the final meshes obtained with the four spatial discretization schemes. The three passes of the refinement procedure have used threshold values $\Gamma = (0.01\ ,\ 0.01\ ,\ 0.01)$ for the solutions with the van Leer scheme and $\Gamma = (0.001\ ,\ 0.001\ ,\ 0.001)$ for the corresponding solutions with the Liou scheme. The experience has shown that it was necessary to have more stringent values of the threshold limit with the Liou scheme than with the van Leer scheme, in order to obtain meshes of comparable refinement. The CFL number used for the van Leer solutions and for the 1st-order Liou scheme was equal to 0.2, while 0.005 was used for the 2nd-order Liou scheme. The 1st pass of the adaptive process was performed at the 500th iteration of the flow solver, whereas the 2nd and 3rd passes were performed on the 1300th and 2500th iteration, respectively. The regions of high gradients were adequately refined by all the schemes. The

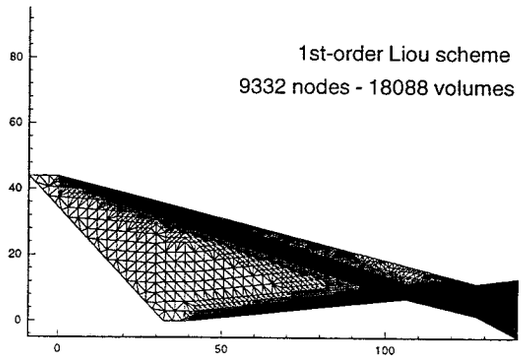

Figure 4: Adaptive mesh obtained using the 1st-order Liou scheme.

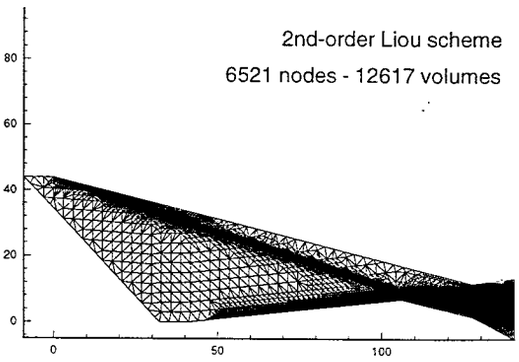

Figure 5: Adaptive mesh obtained using the 2nd-order Liou scheme.

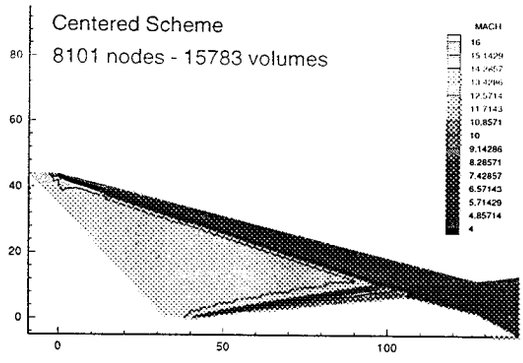

Figure 6: Mach number contours obtained using the 1st-order van Leer scheme ($M_\infty = 16$).

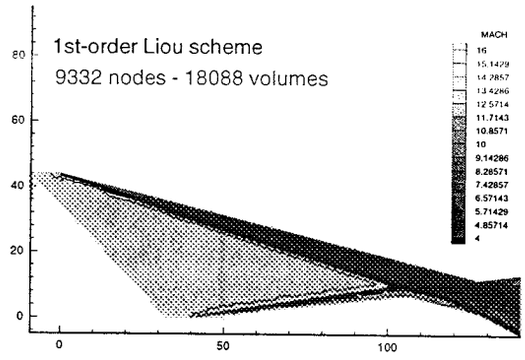

Figure 8: Mach number contours obtained using the 1st-order Liou scheme ($M_\infty = 16$).

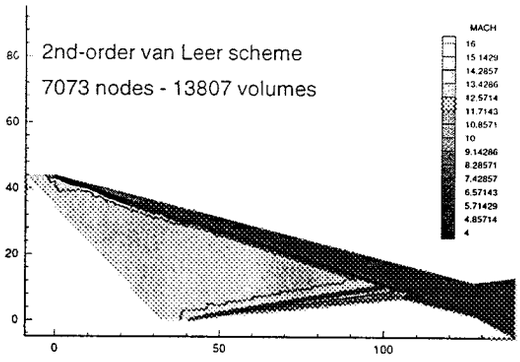

Figure 7: Mach number contours obtained using the 2nd-order van Leer scheme ($M_\infty = 16$).

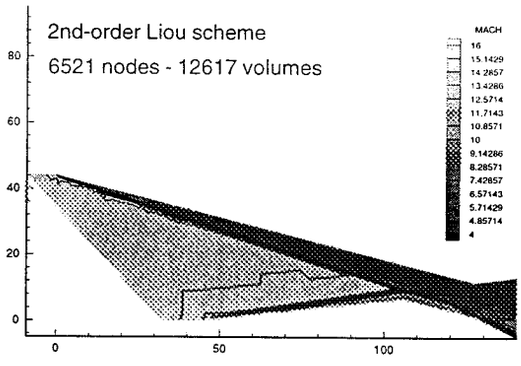

Figure 9: Mach number contours obtained using the 2nd-order Liou scheme ($M_\infty = 16$).

2nd-order van Leer and Liou schemes generated coarser meshes, compared with their 1st-order counterparts. One can also observe that, at the exit of the hypersonic inlet configuration, all the schemes presented a good refined mesh.

The corresponding Mach number contours computed with the schemes are presented in Figures 6, 7, 8 and 9. It is clear that the 1st-order van Leer and Liou schemes smoothed out the spatial gradients by the intrinsic artificial dissipation present in upwind implementation with only 1st-order accuracy. Moreover, the 1st-order van Leer scheme seems to be more dissipative than the 1st-order Liou scheme. The reason for this comment can be clearly seen if one compares the upper and lower wall entrance shock resolution. The 2nd-order Liou scheme achieved the best shock capture in the sense that the shock is the least smeared in comparison with the other methods. On the other hand, this scheme presented the strongest oscillations near the lower wall entrance shock.

One can observe that the phenomena present at the exit of the inlet configuration were well captured by both versions of the Liou scheme. It is clear that more information about the fluid flow in this region can be obtained from Figs. 8 and 9 than from the corresponding results with the van Leer scheme. Moreover, in the region just upstream of the geometric throat, the van Leer scheme presented a different solution than that obtained with the versions of the Liou scheme. This is particularly true if one considers the shock that appears due to the upper and lower shock interaction. Furthermore, the versions of the van Leer scheme could capture the expansion region after the first deflection on the lower wall. The 1st- and 2nd-order versions of the Liou scheme could not detect such phenomenon, and the shock is nearly parallel to the wall.

Viscous Test Cases

In the viscous studies performed in the context of the present work, although the Reynolds number in all simulations was characteristic of turbulent flow regimes, no turbulence model was implemented. This should be seen as a preliminar development stage, in which laminar flow simulations are performed, before attempting to implement appropriate turbulence models. The first test case considered the flow in a transonic convergent-divergent nozzle. The computational mesh was generated by a

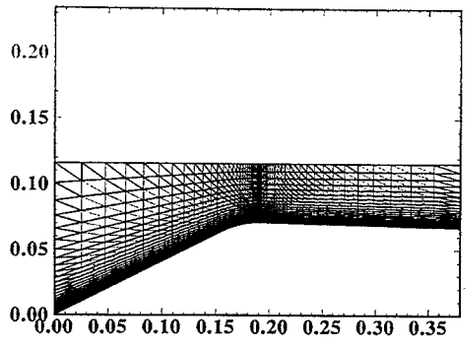

Figure 10: Unstructured mesh for the transonic nozzle problem.

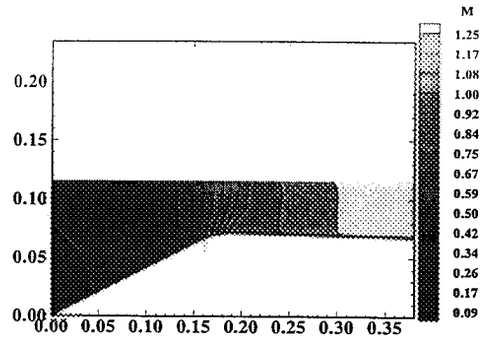

Figure 12: Mach number contours in the transonic nozzle problem.

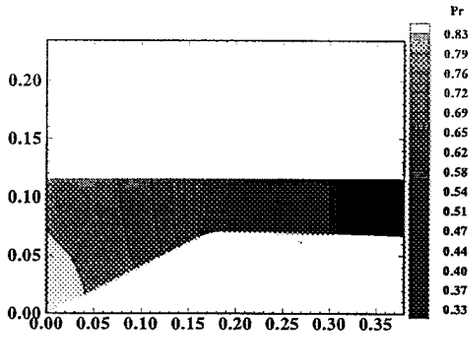

Figure 11: Pressure contours in the transonic nozzle problem.

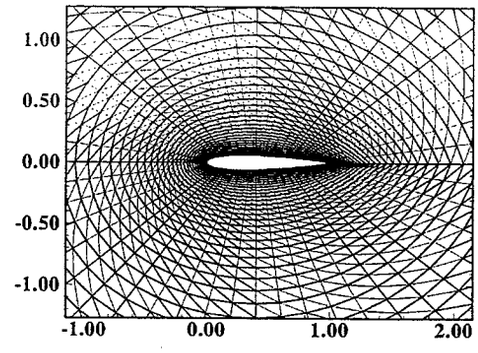

Figure 13: Unstructured mesh for a NACA 0012 airfoil.

structured, algebraic grid generator, with 61 points in the direction along the nozzle axis and 40 points in direction normal to nozzle wall. An exponential stretching with 10% stretching factor was used to cluster grid points towards the nozzle wall and towards the throat. This structured mesh was later triangulated yielding an unstructured grid with 4,680 triangular real volumes and 2,440 nodes. This mesh is shown in Fig. 10.

Stagnation conditions were used as initial conditions for the present simulation for the complete domain, except at the exit boundary where a reduction in pressure and density was imposed in order to initialize the flow. The exit pressure was set low enough in order to obtain supersonic flow in the nozzle divergent section. The Reynolds number was set to 1 million and the Prandtl number was selected as 0.72. Figure 11 presents the pressure contours obtained with the centered scheme previously described. It is possible to observe that the weak shock wave near the throat is well captured by the method, without the need for any modification in the artificial dissipation coefficient values. This is an evidence of the accurate behavior of artificial dissipation operator implemented. Figure 12 shows the Mach number contours obtained with the same scheme. Results are in good agreement with available experimental results, again emphasizing the good features of the artificial dissipation operator in avoiding competition between artificial dissipation and natural dissipation.

The next case considered transonic flow over a NACA 0012 airfoil. The mesh was also generated as an structured, O-type mesh, with 49×60 grid points in the wrap-around and wall-normal directions, respectively. An exponential stretching with 10% stretching factor was used in the wall normal direction. After triangulation, this has yielded 5,664 triangular real volumes and 2,940 nodes. This unstructured mesh is shown in Fig. 13. The far field was located at 25 chords lengths from the airfoil.

In this case, the freestream Mach number was set to 1.0 and the angle of attack was set to zero. The Reynolds number was selected as 10 million, and the Prandtl number was also set to 0.72. Pressure and mach number contours obtained for the solution with the centered scheme are presented, respectively, in Figs. 14 and 15. Since the flow conditions in the present case are more severe than those of the transonic nozzle problem, there was a need to modify the $K^{(2)}$ and $K^{(4)}$ artificial dissipation coefficients with respect to the standard values suggested in the literature[2]. The values adopted in the present case

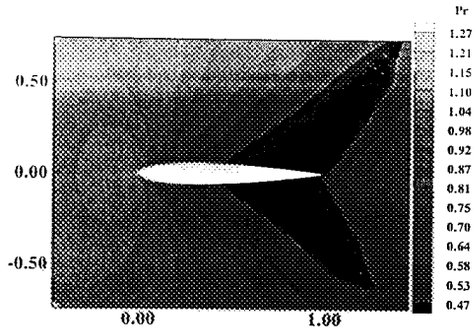

Figure 14: Pressure contours for the NACA 0012 airfoil problem ($M_\infty = 1.0$ and $Re = 10$ million).

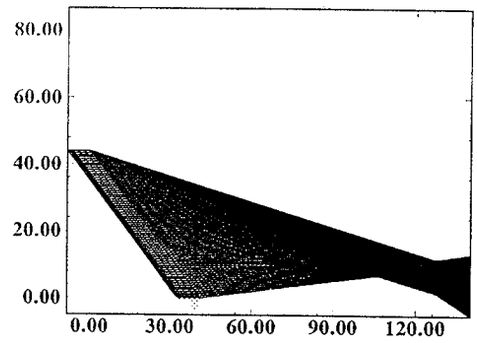

Figure 16: Computational grid used for viscous simulations of the hypersonic inlet case.

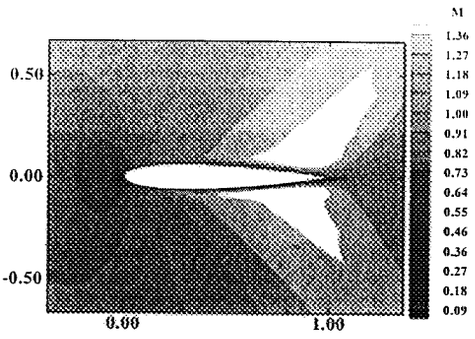

Figure 15: Mach number contours for the NACA 0012 airfoil problem ($M_\infty = 1.0$ and $Re = 10$ million).

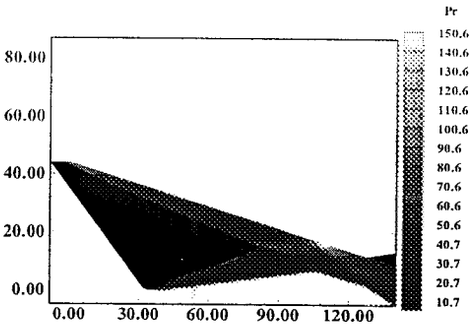

Figure 17: Pressure contours for viscous simulation of the hypersonic inlet problem ($M_\infty = 15$ and $Re = 10^5$).

were $K^{(2)} = 0.4$ and $K^{(4)} = 0.03$. This amount of artificial dissipation was necessary to guarantee a stable convergence to steady state without introducing too much degradation of the global solution quality.

The final test case simulated with a viscous formulation considered the same hypersonic inlet discussed in the previous section. In this case, a mesh with 4,900 grid points and 19,044 triangular elements was generated. This mesh is shown in Fig. 16. Flight conditions for the present simulation considered an entrance (freestream) Mach number $M_\infty = 15$ and the flow aligned with the inlet axis. The Reynolds number, based on the total inlet length, was set to 1.0×10^5, which is consistent with flight at approximately 35 km. This simulation also assumed $Pr = 0.72$. As previously discussed, the present simulation has not considered any real gas effects which certainly would occur for flight at such extreme conditions. Hence, this should be seen as cold gas hypersonic simulations for an evolutionary validation of the capability implemented.

From the numerical point of view, the hypersonic inlet case represented a much more severe test case, as also discussed in the context of the inviscid simulations. For the viscous results here reported, the CFL number was selected as 0.1. The centered scheme was still used in this case, but it was necessary to increase the artificial dissipation model constants to $K^{(2)} = 0.65$ and $K^{(4)} = 0.04$, in order to maintain numerical stability. Pressure and Mach number contours for this simulation are presented in Figs. 17 and 18, respectively. One can see from these figures that there is a good qualitative agreement of the overall inviscid features of the flow between the inviscid results previously discussed and the present calculations, although the former have been computed with upwind schemes.

Clearly, however, the viscous simulations allow for further study of the flow in the inlet. In particular, the viscous calculations have indicated that there is flow separation on the lower inlet wall. A fairly distinctive separation bubble on the lower wall can be seen in Figs. 19 and 20, which present velocity vector plots for this solution. These results seem to indicate that the flow separation is somehow coupled to the shock-shock interaction phenomenon which occurs further downstream along the inlet, at the location in which the separation bubble has its largest dimension in the crossflow direction. The additional details of the separated region along the lower inlet

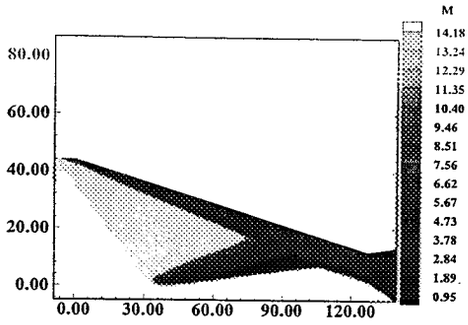

Figure 18: Mach number contours for viscous simulation of the hypersonic inlet problem ($M_\infty = 15$ and $Re = 10^5$).

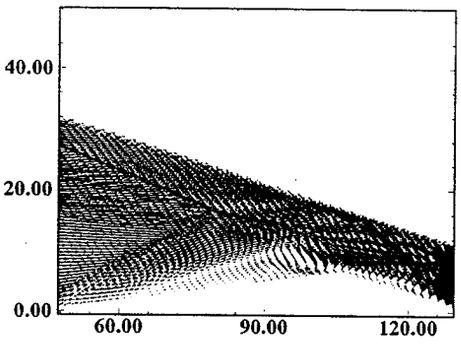

Figure 19: Flow separation along the lower wall in the hypersonic inlet problem ($M_\infty = 15$ and $Re = 10^5$).

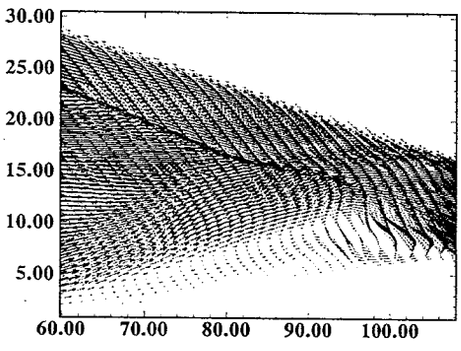

Figure 20: Detail of flow separation upstream of first expansion corner along the lower wall in the hypersonic inlet configuration ($M_\infty = 15$ and $Re = 10^5$).

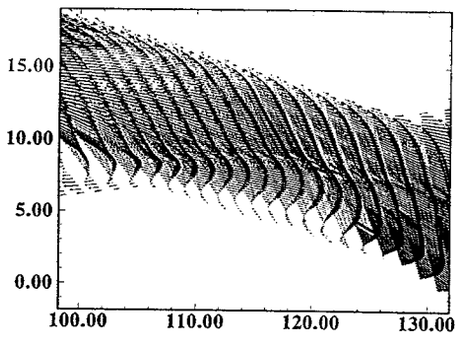

Figure 21: Detail of flow separation downstream of first expansion corner along the lower wall in the hypersonic inlet configuration ($M_\infty = 15$ and $Re = 10^5$).

wall, shown in Fig. 20, were obtained by zooming on the region just upstream of the first expansion corner on the lower wall. The shock-shock interaction region is clearly seen in Figs. 19 and 20. Moreover, the fairly strong recirculation region which is formed just underneath this interaction is also evident from Fig. 20. The corresponding expanded view of the region downstream of this first lower wall expansion corner can be seen in Fig. 21. These figures also show that there is a considerable reduction in the lateral extension of the separation bubble at the first lower wall expansion corner. Further downstream of this point, the crossflow extension of the separation bubble again increases and the flow finally reattaches at the second lower wall expansion corner. One should observe, however, that the present calculations are laminar Navier-Stokes simulations. Therefore, flow separation characteristics could be rather different if a turbulence model were implemented in the code.

Concluding Remarks

The present work performed the implementation and validation of unstructured grid, mesh refinement techniques for 2-D inviscid and viscous flow simulations. The governing equations were discretized in an unstructured triangular mesh by a cell centered finite volume algorithm. The equations were advanced in time by an explicit, 5-stage, 2nd-order accurate, Runge-Kutta time stepping procedure. The spatial discretization considered a central difference-type scheme and two upwind schemes, namely a van Leer and a Liou flux-vector splitting schemes with both 1st- and 2nd-order implementations.

The inviscid results were obtained for cold gas flow in a hypersonic inlet. The tests performed considered the comparison of the results obtained with the four different upwind spatial discretizations schemes for this problem. The inlet entrance conditions were $M_\infty = 16$ and flow aligned with the inlet axis. Moreover, the fluid was treated as a perfect gas. Clearly, for actual flight condition simulation, real gas effects would have to be taken

into account. Here, however, the consideration of very high Mach number flows had simply the objective of testing the behavior of the different schemes in the presence of strong shocks.

The implementation of the 2nd-order versions of the two upwind schemes used MUSCL reconstruction in order to obtain left and right states at each interface. The 2nd-order versions of the upwind schemes require the implementation of limiters in order to try to minimize oscillations at discontinuities. A few different limiters were actually coded, but only results with the minmod limiter were reported here. The 1st-order methods caused considerable smearing of the flow discontinuities due to the excessive artificial dissipation intrinsically added. Among the various schemes implemented, the 2nd-order upwind methods have provided the best shock capturing capability. The shock resolution obtained with the 2nd-order Liou scheme was slightly better than that provided by the 2nd-order van Leer method. The mesh adaptation procedure implemented was able to generate good quality meshes for the inviscid cases considered in the present work.

Viscous simulations have considered airfoil flows, transonic convergent-divergent nozzle cases and the hypersonic inlet configuration. All cases were run using the central difference-type spatial discretization scheme. The results obtained were quite encouraging, since all calculations have shown good qualitative agreement with the expected flow features. Clearly, further work and validation are still necessary in the viscous cases. In particular, testing of the adaptive refinement capability in the viscous cases and the implementation of adequate turbulence models are the next steps in the continuation of the present development effort.

Acknowledgments

The authors gratefully acknowledge the support of Conselho Nacional de Desenvolvimento Científico e Tecnológico, CNPq, and of Fundação de Amparo à Pesquisa do Estado de São Paulo, FAPESP, through doctoral scholarships for the first and second authors, respectively. The present work was also partially supported by CNPq under the Integrated Project Research Grant No. 522413/96-0.

References

1. Jameson, A., and Mavriplis, D., "Finite Volume Solution of the Two-Dimensional Euler Equations on a Regular Triangular Mesh," *AIAA Journal*, Vol. 24, No. 4, April 1986, pp. 611-618.
2. Mavriplis, D.J., "Multigrid Solution of the Two-Dimensional Euler Equations on Unstructured Triangular Meshes," *AIAA Journal*, Vol. 26, No. 7, July 1988, pp. 824-831.
3. van Leer, B., "Flux-Vector Splitting for the Euler Equations," *Proceedings of the 8th International Conference on Numerical Methods in Fluid Dynamics*, E. Krause, editor, *Lecture Notes in Physics*, Vol. 170, pp. 507-512, Springer-Verlag, Berlin, 1982.
4. Anderson, W.K., Thomas, J.L., and van Leer, B., "A Comparison of Finite Volume Flux Vector Splittings for the Euler Equations," *AIAA Journal*, Vol. 24, Sept. 1986, pp. 1453-1460.
5. Liou, M.-S., "A Continuing Search for a Near-Perfect Numerical Flux Scheme. Part I: AUSM$^+$," NASA TM-106524, NASA Lewis Research Center, Cleveland, OH, Mar. 1994.
6. Liou, M.-S.,"A Sequel to AUSM: AUSM$^+$," *Journal of Computational Physics*, Vol. 129, 1996, pp. 364-382.
7. van Leer, B., "Towards the Ultimate Conservative Difference Scheme. V. A Second-Order Sequel to Godunov's Method," *Journal of Computational Physics*, Vol. 32, No. 1, July 1979, pp. 101-136.
8. Hirsch, C., *Numerical Computation of Internal and External Flows. Vol. 2: Computational Methods for Inviscid and Viscous Flows*, Wiley, New York, 1990 (Chapt. 20, pp. 408-443).
9. Jameson, A., Schmidt, W., and Turkel, E., "Numerical Solution of the Euler Equations by Finite Volume Methods Using Runge-Kutta Time-Stepping Schemes," AIAA Paper 81-1259, AIAA 14th Fluid and Plasma Dynamics Conference, Palo Alto, CA, June 1981.
10. Azevedo, J.L.F., "On the Development of Unstructured Grid Finite Volume Solvers for High Speed Flows," Report NT-075-ASE-N/92, Instituto de Aeronáutica e Espaço, CTA/IAE/ASE, São José dos Campos, SP, Dec. 1992.
11. Azevedo, J.L.F., and Korzenowski, H., "Comparison of Unstructured Grid Finite Volume Methods for Cold Gas Hypersonic Flow Simulations," AIAA Paper No. 98-2629, to appear in the *Proceedings of the 16th AIAA Applied Aerodynamics Conference*, Albuquerque, NM, June 1998.
12. Azevedo, J.L.F., and Figueira da Silva, L.F., "The Development of an Unstructured Grid Solver for Reactive Compressible Flow Applications," AIAA Paper 97-3239, 33rd AIAA/ASME/SAE/ASEE Joint Propulsion Conference & Exhibit, Seattle, WA, July 1997.
13. Mavriplis, D.J., "Accurate Multigrid Solution of the Euler Equations on Unstructured and Adaptive Meshes," *AIAA Journal*, Vol. 28, No. 2, Feb. 1990, pp. 213-221.
14. Swanson, R.C., and Radespiel, R., "Cell Centered and Cell Vertex Multigrid Schemes for the Navier-Stokes Equations," *AIAA Journal*, Vol. 29, No. 5, May 1991, pp. 697-703.